



**HAL**  
open science

# Biaxial Testing of Sheet Materials at High Strain Rates Using Viscoelastic Bars

Vincent Grolleau, Gérard Gary, Dirk Mohr

► **To cite this version:**

Vincent Grolleau, Gérard Gary, Dirk Mohr. Biaxial Testing of Sheet Materials at High Strain Rates Using Viscoelastic Bars. *Experimental Mechanics*, 2008, 48 (3), pp.293-306. 10.1007/s11340-007-9073-5 . hal-00171907

**HAL Id: hal-00171907**

**<https://hal.science/hal-00171907>**

Submitted on 13 May 2018

**HAL** is a multi-disciplinary open access archive for the deposit and dissemination of scientific research documents, whether they are published or not. The documents may come from teaching and research institutions in France or abroad, or from public or private research centers.

L'archive ouverte pluridisciplinaire **HAL**, est destinée au dépôt et à la diffusion de documents scientifiques de niveau recherche, publiés ou non, émanant des établissements d'enseignement et de recherche français ou étrangers, des laboratoires publics ou privés.

# Biaxial Testing of Sheet Materials at High Strain Rates Using Viscoelastic Bars

V. Grolleau · G. Gary · D. Mohr

**Abstract** A dynamic bulge testing technique is developed to perform biaxial tests on metals at high strain rates. The main component of the dynamic testing device is a movable bulge cell which is directly mounted on the measuring end of the input bar of a conventional split Hopkinson pressure bar system. The input bar is used to apply and measure the bulging pressure. The experimental system is analyzed in detail and the measurement accuracy is discussed. It is found that bars made of low impedance materials must be used to achieve a satisfactory pressure measurement accuracy. A series of dynamic experiments is performed on aluminum 6111-T4 sheets using viscoelastic nylon bars to demonstrate the capabilities of the proposed experimental technique. The parameters of the rate-dependent Hollomon–Cowper–Symonds J2 plasticity model of the aluminum are determined using an inverse analysis method in conjunction with finite element simulations.

**Keywords** Bulge test · Biaxial experiments · Rate-dependent plasticity · Split Hopkinson pressure bar apparatus · High strain rates

---

V. Grolleau  
Laboratoire Génie Mécanique et Matériaux,  
Université de Bretagne Sud,  
Lorient, France

G. Gary · D. Mohr  
Solid Mechanics Laboratory (CNRS-UMR 7649),  
Department of Mechanics, École Polytechnique,  
Palaiseau, France

D. Mohr  
Impact and Crashworthiness Laboratory,  
Department of Mechanical Engineering,  
Massachusetts Institute of Technology,  
77 Massachusetts Avenue,  
Cambridge, MA 02139, USA  
e-mail: mohr@mit.edu

## Introduction

This paper deals with the design of a dynamic bulge testing device for the biaxial testing of sheet metal specimens. In a conventional bulge test, the so-called bulge is formed by applying a high pressure loading through a liquid on one side of a fully-clamped sheet specimen (Fig. 1). Bulge tests are typically performed to study the large deformation behavior of solids under biaxial loading conditions. When testing highly ductile Levy–von Mises solids, necking occurs later under biaxial than under uniaxial conditions; as a result, the characteristic stress–strain curve can be determined over a wider range of strains.

The basic quasi-static bulge testing technology was developed in the late 1940's to investigate the plasticity [6] and strength of sheet metal (e.g. [3]). This early experimental work was complemented by several theoretical treatises (e.g. Hill [8] and Ross and Prager [20]). The quasi-static bulge test has become an established experimental technique to determine the elastic, plastic and failure properties of materials under biaxial stress states. For example, the bulge test has been employed to identify the biaxial strain hardening laws for sheet materials [1, 4, 7, 16] as well as to investigate the elastic properties of thin films (e.g. [12, 22, 23]). Another important application of the bulge test is the determination of forming limit diagrams of sheet metal [11, 17]. In particular, bulge tests with elliptical dies have been developed to control and vary the strain path to failure under biaxial loading [2, 18].

Broomhead and Grieve [2] made use of the bulge test to study the effect of strain rate on the strain to fracture of sheets subject to biaxial tension. Their drop hammer rig makes use of a falling weight to impact a punch which in turn applies a pressure loading to the fluid above the sheet material. A pressure transducer is used for the load measurement while the strains are measured post-mortem. Using

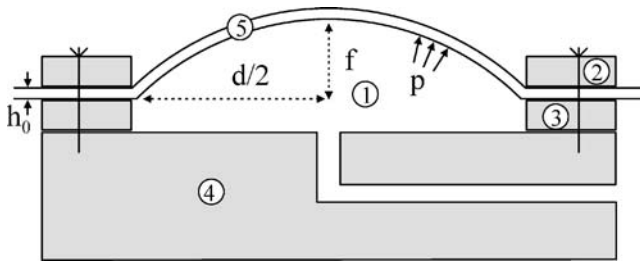


**Fig. 1** System for static bulge testing: (1) high pressure chamber, (2) die ring, (3) back ring, (4) base plate, (5) bulged sheet specimen

this set-up, they determined the forming limit curves of low carbon steel for strain rates of up to  $70 \text{ s}^{-1}$ . Pickett et al. [15] made use of a similar rig to measure the high strain rate response of high strength steels.

In the present work, we propose an adaptation of the split Hopkinson pressure bar (SHPB) apparatus to measure the pressure and velocities in a dynamic bulge test. It is shown that a set of viscoelastic nylon bars in conjunction with a specially-designed bulge cell provides a reliable measurement system for the biaxial dynamic testing at strain rates of up to  $500 \text{ s}^{-1}$ . “Dynamic Bulge Testing System” gives a brief general overview of the proposed dynamic bulging system. The mechanics of bulge testing are discussed in “Theoretical Analysis”, before dynamic experiments on aluminum 6111-T4 sheets are presented in “Experiments”. The material model parameters describing the rate-dependency of the tested aluminum sheets are determined through inverse analysis; “Numerical Simulations and Inverse Analysis” outlines the inverse analysis procedure and provides details on the underlying finite element model. Limitations and possible enhancements of the proposed hybrid experimental-numerical technique are discussed in “Discussion”, followed by a short conclusion in “Conclusion”. It shall be noted that the present paper focuses on the development of the experimental technique. Conversely, only little background is given on the material model identification procedure through inverse analysis.

## Dynamic Bulge Testing System

### Background

In conventional *static* bulge tests, a sheet specimen is sandwiched between two thick steel rings (so-called back and die rings). This sub-assembly is then bolted onto the top of an oil-filled cylindrical high pressure chamber (Fig. 1). The sheet is formed into a bulge by gradually increasing the oil pressure. Both the oil pressure and the oil influx are measured throughout the experiments which allows for the determination of the biaxial stresses and strains at the center of the sheet using approximate analytical formulas. In some

instances, the curvature is measured in order to improve the stress and strain estimates. Furthermore, the strains may be measured directly on the sheet surface through the use of strain gages or optical techniques.

### Dynamic Testing System

We propose a new bulge testing device to perform dynamic bulge tests in a SHPB system. In a conventional SHPB system, the specimen is placed between the so-called input and output bars while a striker bar is used to generate the dynamic pressure loading [Fig. 2(a)]. Here, the idea is to design a movable “bulge cell” which can be used to perform dynamic bulge tests in a SHPB system. Figure 2(b) shows a schematic of the bulge cell including all part numbers. Its special feature is the integration of the input bar (part #4) into the testing device. The bulge cell is composed of a thick-walled steel cylinder (part #3) and a die ring (part #2). For testing, the round sheet specimen (part #5) of thickness  $h_0$  is clamped between the cylinder and the die ring. The input bar is inserted into the cylindrical cell and a fluid (part #1) is filled into the cell to transmit the pressure from the input bar to the sheet surface. The outer diameter of the input bar matches the inner diameter of the cell. The tubular cross-section of the output bar (part #6) is chosen such that it matches the contact surface of the die ring.

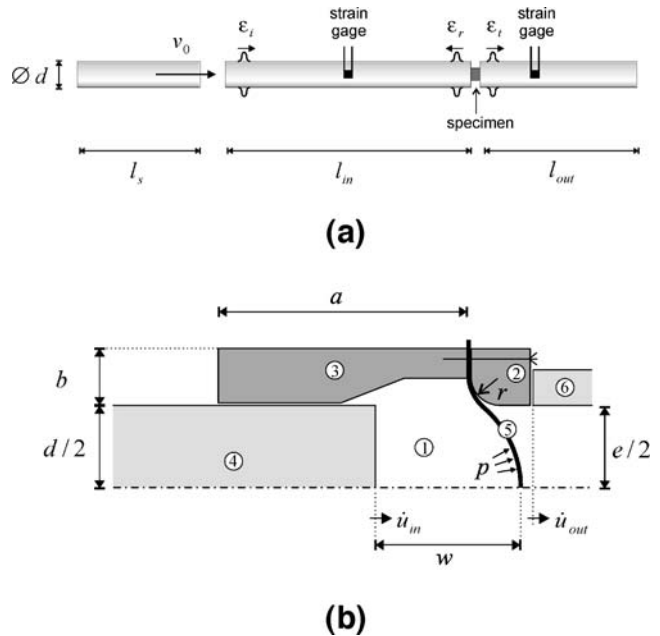


**Fig. 2** (a) Conventional SHPB system; (b) axisymmetric bulge cell for dynamic testing composed of (1) fluid, (2) die ring, (3) thick-walled cylinder, (4) input bar, (5) sheet specimen, (6) tubular end of the output bar

When the striker bar impacts the input bar at a velocity  $v_0$ , a pressure wave is generated propagating towards the input bar/fluid interface. This pressure wave is transmitted through the fluid and ultimately causes the bulging of the sheet specimen while both the bulge cell and the output bar are accelerated. Throughout each experiment, the incoming and reflected waves are measured by strain gages positioned near the center of the input bar [Fig. 2(a)]. Furthermore, the so-called transmitted wave is measured by strain gages positioned on the output bar.

#### Determination of the Bulging Pressure and Displacement

Unlike in classical SHPB analysis, we make use of the input bar to measure the bulging pressure. The fluid pressure in the bulge cell  $p(t) \geq 0$  is determined directly from the incident axial strain wave  $\varepsilon_i(t)$  and the reflected axial strain wave  $\varepsilon_r(t)$  at the input bar/fluid interface:

$$p(t) = -E_{in}[\varepsilon_i(t) + \varepsilon_r(t)]. \quad (1)$$

The corresponding input bar/fluid interface velocity reads

$$\dot{u}_{in}(t) = c_{in}[-\varepsilon_i(t) + \varepsilon_r(t)]. \quad (2)$$

$c_{in} = \sqrt{E_{in}/\rho_{in}}$  is the one dimensional elastic wave speed in the input bar, where  $E_{in}$  and  $\rho_{in}$  denote the Young's modulus and mass density of the input bar material. Analogously, the notation  $c_{out}$ ,  $E_{out}$  and  $\rho_{out}$  is used for the properties of the output bar material (which may be different from the input bar material). The velocity of the bulge cell  $\dot{u}_{out}(t)$  [Fig. 2(b)] is determined from the transmitted wave  $\varepsilon_{tra}(t)$  at the output bar/die ring interface,

$$\dot{u}_{out}(t) = -c_{out}\varepsilon_{tra}(t). \quad (3)$$

The effective piston velocity ( $\Delta\dot{u} > 0$  for compression) corresponds to the difference of the interface velocities,

$$\Delta\dot{u} = \dot{u}_{in}(t) - \dot{u}_{out}(t). \quad (4)$$

Upon integration of this relationship, we obtain the effective piston displacement as a function of the measured strain histories:

$$\Delta u(t) = c_{in} \int_t [-\varepsilon_i(\tau) + \varepsilon_r(\tau)] d\tau + c_{out} \int_t \varepsilon_t(\tau) d\tau. \quad (5)$$

#### Theoretical Analysis

A theoretical analysis is performed for rate-independent sheet materials to provide insight in the dynamics of the testing system. A dynamic experiment with SHPBs is neither a displacement-controlled nor a force-controlled experiment.

The magnitude of the maximum forces and displacements can be controlled, but not the exact displacement- or force-time histories; both time-histories depend on the mechanical response of the specimen and the bars. Thus, the pressure-displacement relationship of a bulging specimen is derived first, before analyzing the entire testing system and deriving an explicit formula to estimate the equivalent plastic strain rate. Furthermore, the accuracy of the force measurement is discussed. A brief summary of the main conclusions drawn from this theoretical analysis is given in "Summary".

#### Pressure-displacement Relationship

We briefly recall some results from Hill's analysis [8] of the static bulge test. Assuming a small thickness-to-diameter ratio,  $h_0/d \ll 1$ , the sheet specimen is considered as a membrane subject to large deformations. Furthermore, the analysis is restricted to rigid-plastic Levy-von Mises materials with isotropic strain hardening. The key kinematic simplification is to assume that the sheet is deformed into a spherical cap (Fig. 1). For this special geometry, the sheet material is uniformly stretched; both membrane strain components (the incremental plastic circumferential strain  $d\varepsilon_{\theta\theta}^p$  and the hoop strain  $d\varepsilon_{\varphi\varphi}^p$ ) are equal. Moreover, under monotonic loading, the equivalent plastic strain  $\bar{\varepsilon}_p$  is given by the relationship

$$\bar{\varepsilon}_p = 2\varepsilon_{\theta\theta}^p = 2\varepsilon_{\varphi\varphi}^p = 2 \ln \left[ 1 + \left( \frac{2f}{d} \right)^2 \right]. \quad (6)$$

where  $f \geq 0$  denotes the polar height of the bulge (Fig. 1). Recall that  $d$  denotes the inner die ring diameter which remains constant throughout bulging.

The bulging pressure  $p = p(s, f) \geq 0$  is a function of both the current bulge geometry, (i.e. the polar height  $f$ ) and the current deformation resistance of the Levy-von Mises sheet material,  $s = s(\bar{\varepsilon}_p) \geq 0$ . For spherical bulges, the expression for the bulging pressure reads

$$p = \frac{h_0}{d} g(\bar{\varepsilon}_p) s(\bar{\varepsilon}_p) \quad (7)$$

where

$$g(\bar{\varepsilon}_p) = 8 \sqrt{\frac{\exp(0.5\bar{\varepsilon}_p) - 1}{\exp(3\bar{\varepsilon}_p)}}. \quad (8)$$

This result implies that for a given material, the ratio of the sheet thickness to the bulge diameter,  $h_0/d$ , is the only geometrical variable that determines the bulging pressure. The function  $g(\bar{\varepsilon}_p)$  increases monotonically for small strains, while it reaches a plateau value of about  $g(\bar{\varepsilon}_p) \cong 2.0$  for strains greater than  $\bar{\varepsilon}_p \geq 0.2$ . In other words, for strains larger than  $\bar{\varepsilon}_p \geq 0.2$ , the bulging pressure is no

longer affected by the evolving geometry (increasing depth/curvature and sheet thickness reduction). Instead, it is directly proportional to the deformation resistance of the sheet material. The above result also shows that in a typical bulge test, the pressure level is usually of the order of a few percent of the material's yield strength.

Upon further evaluation of the kinematics of Hill's model, we can express the effective piston displacement as a function of the equivalent plastic strain:

$$\frac{\Delta u}{d} = \frac{1}{12} [2 + \exp(0.5\bar{\epsilon}_p)] \sqrt{\exp(0.5\bar{\epsilon}_p) - 1}. \quad (9)$$

Using equations (7) to (9) and assuming a constant yield stress  $s(\bar{\epsilon}_p) = s_0$ , we plotted the normalized bulging pressure  $p/s_0$  as a function of the normalized piston displacement  $\Delta u/d$  (Fig. 3). The solid curve in Fig. 3 represents the characteristic specimen response in a bulge test. For a rigid-plastic material, the pressure level in a bulge test increases continuously until a plateau level is reached when the equivalent plastic strains are larger than about 0.2. It is emphasized that this intrinsic response curve cannot be changed by manipulating the specimen geometry.

#### Plastic Strain Rate

An approximate relationship is derived to estimate the equivalent plastic strain rate and to gain further insight in the mechanics of the dynamic bulge testing system. For simplicity, we assume an ideal elastic SHPB system (flat contact surfaces, perfect alignment, dispersion free) and a rigid-plastic sheet material of constant deformation resistance

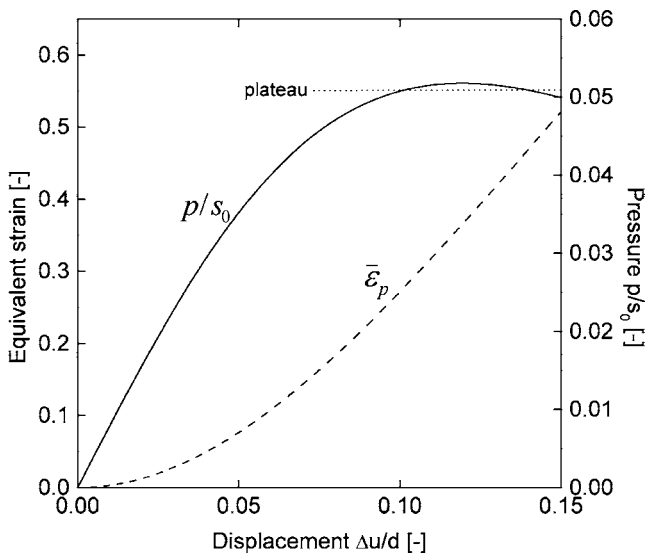


**Fig. 3** Normalized bulging pressure (solid line) and equivalent plastic strain (dashed line) for  $d/h_0=40$  as a function of the normalized piston displacement

$s(\bar{\epsilon}_p) = s_0$ . Furthermore, we restrict our analysis to large strains where the bulging pressure may be approximated by

$$p(t) \cong p_0 = \frac{2h_0}{d} s_0 \quad (10)$$

In a standard SHPB experiment, the striker bar hits the input bar at a known velocity  $v_0$  which generates the incident wave of the strain magnitude

$$\epsilon_i = -\frac{v_0}{2c_{in}} \quad (11)$$

which propagates towards the input bar/specimen interface. At this interface, this wave is partially reflected where the amplitude of the reflected tensile wave  $\epsilon_r$  depends on the specimen resistance. Combining equations (1), (10) and (11), we have

$$\epsilon_r = \frac{v_0}{2c_{in}} - \frac{p_0}{E_{in}} \quad (12)$$

Note that the striker velocity  $v_0$  must be greater than the minimum velocity  $v_{min}$ ,

$$v_{min} = 2c_{in} \frac{p_0}{E_{in}} \quad (13)$$

in order to deform the sheet material plastically. The corresponding interface velocity  $\dot{u}_{in}$  is

$$\dot{u}_{in}(t) = c_{in}[-\epsilon_i + \epsilon_r] = v_0 - c_{in} \frac{p_0}{E_{in}} \quad (14)$$

In a similar way, we can derive an expression for the velocity of the interface between the output bar and the bulge cell. Neglecting the inertia and compressibility of the fluid as well as the inertia of the sheet, the equilibrium of forces at the output bar interface reads

$$A_{in}p_0 + A_{out}E_{out}\epsilon_t(t) = M\ddot{u}_{out}(t) \quad (15)$$

Furthermore, we consider the bulge cell as a rigid body of mass  $M$ ; the acceleration of the output bar interface is denoted by  $\ddot{u}_{out}(t)$ , while  $A_{in}=\pi d^2/4$  and  $A_{out}$  denote the cross-sectional areas of the input bar and output bar, respectively. The strain  $\epsilon_t(t)$  in the output bar is proportional to the interface velocity,

$$\epsilon_t(t) = -\frac{\dot{u}_{out}(t)}{c_{out}} \quad (16)$$

Combining equations (15) and (16) yields a differential equation for  $\dot{u}_{out}(t)$  with the solution

$$\dot{u}_{out}(t) = \frac{p_0}{\sqrt{\rho_{out}E_{out}}} \times \frac{A_{in}}{A_{out}} \left[ 1 - \exp\left(-\frac{\sqrt{\rho_{out}E_{out}}A_{out}}{M}t\right) \right]. \quad (17)$$

The effective piston velocity reads

$$\begin{aligned} \Delta \dot{u}(t) &= \dot{u}_{in}(t) - \dot{u}_{out}(t) = \\ &= v_0 - \frac{p_0}{\sqrt{\rho_{in} E_{in}}} \left\{ 1 + \frac{\sqrt{\rho_{in} E_{in} A_{in}}}{\sqrt{\rho_{out} E_{out} A_{out}}} \right. \\ &\quad \left. \times \left[ 1 - \exp\left(-\frac{\sqrt{\rho_{out} E_{out} A_{out}}}{M} t\right) \right] \right\} \end{aligned} \quad (18)$$

Unlike the input velocity, which remains constant for  $p_0 = \text{const}$ , the output velocity varies in time due to the inertia of the bulge cell. In order to achieve high effective piston velocities, the output velocity should be negligibly small. As described by equation (17), there are basically two strategies to reduce the output velocity: one can either increase the impedance of the output bar (the term  $\sqrt{\rho_{out} E_{out} A_{out}}$ ) or increase the mass  $M$  of the bulge cell.

The plastic strain rate can be related to  $\Delta \dot{u}$  by taking the time derivative of equation (9). However, for  $\bar{\varepsilon}_p > 0.2$ , the non-linear relationship between the equivalent plastic strain and the effective piston displacement may be approximated by a linear function

$$\dot{\bar{\varepsilon}}_p \cong 4.9 \frac{\Delta \dot{u}}{d} \quad (19)$$

Thus, by combining equations (18) and (19), we obtain the estimate of the equivalent plastic strain rate for large strains

$$\dot{\bar{\varepsilon}}_p \cong 4.9 \frac{v_0}{d} \left\langle 1 - \frac{v_{\min}}{2v_0} \left\{ 1 + \frac{\sqrt{\rho_{in} E_{in} A_{in}}}{\sqrt{\rho_{out} E_{out} A_{out}}} \right. \right. \\ \left. \left. \times \left[ 1 - \exp\left(-\frac{\sqrt{\rho_{out} E_{out} A_{out}}}{M} t\right) \right] \right\} \right\rangle \quad (20)$$

The term in angle brackets varies between 0 and 1, depending on the testing configuration, while the factor  $4.9 v_0/d$  may be considered as the governing term in equation (20). In other words, the ratio  $v_0/d$  determines the order of magnitude of the plastic strain rate in a dynamic bulge test. For comparison, in a conventional SHPB compression test on ideal plastic cylindrical specimens, the strain rate is governed by the impact velocity-to-height ratio. Since the height of a conventional specimen is about one to two orders of magnitude smaller than the diameter of a bulge specimen, extremely high striker velocities would be needed in a bulge test to attain similar strain rates as in conventional SHPB experiments.

#### Accuracy of the Pressure Measurement

As expressed by equation (1), the fluid pressure is proportional to the sum of the strain gage measurements  $\varepsilon_i(t)$  and  $\varepsilon_r(t)$ . In order to assess the pressure measurement accuracy, we suppose that the accuracy of each strain measurement may be characterized by the standard uncertainty  $\delta\varepsilon$  (here,

the standard uncertainty is defined as the square root of the statistical variance,  $\delta\varepsilon = \sqrt{\text{Var}(\varepsilon)}$ , NIST [13]). Since the measurements  $\varepsilon_i(t)$  and  $\varepsilon_r(t)$  are independent, the variance of the normalized pressure measurement reads

$$\text{Var}\left(\frac{p}{E_{in}}\right) = \text{Var}(\varepsilon_i) + \text{Var}(\varepsilon_r) \quad (21)$$

Hence, we have the standard uncertainty of the pressure measurement

$$\delta p = \sqrt{2} E_{in} \delta\varepsilon \quad (22)$$

The strain gages are typically used in a range where the relative uncertainty is very small, i.e.

$$\frac{\delta\varepsilon}{|\varepsilon_i|} \ll 1 \quad (23)$$

However, in the SHPB experiment we have  $\varepsilon_i(t) \leq 0$  and  $|\varepsilon_r(t)| \leq -\varepsilon_i(t)$ ; thus, the uncertainty with respect to the sum of these two strain signals may become considerably large. More specifically, the relative uncertainty in the pressure measurement reads

$$\frac{\delta p}{|p|} = \frac{\sqrt{2} \delta\varepsilon}{|\varepsilon_i + \varepsilon_r|} = \frac{\sqrt{2}}{1 + \chi} \frac{\delta\varepsilon}{|\varepsilon_i|} \quad (24)$$

where the parameter  $\chi = \varepsilon_r/\varepsilon_i$ ,  $|\chi| \leq 1$ , denotes the ratio of the reflected to the incident wave. Clearly, the relative uncertainty in the measured pressure is significantly larger than the relative uncertainty in the measurement of the incoming wave. In particular, we have  $\delta p \rightarrow \infty$  for very soft specimens where  $\chi \rightarrow -1$ . Due to its dependency on the characteristic response function of the specimen, the ratio  $\chi$  changes throughout the experiment. According to the simple mechanical model presented above [equations (1) and (11)], we have

$$\chi = -1 + \frac{2p(t)}{v_0 \sqrt{E_{in} \rho_{in}}} \quad (25)$$

It may be concluded from equations (24) and (25) that the smaller the impedance  $\sqrt{E_{in} \rho_{in}}$  of the input bar material the greater the accuracy of the pressure measurement.

#### Summary

The following conclusions may be drawn from the theoretical analysis:

- (i) The bulging pressure is about two orders of magnitude smaller than the yield strength of the sheet material;
- (ii) the sheet thickness-to-bulge diameter ratio,  $h_0/d$ , is the only geometrical variable that influences the bulging pressure;

- (iii) the effective piston displacement for a given equivalent plastic strain is proportional to the bulge diameter;
- (iv) an upper bound for the plastic strain rate is given by  $\bar{\epsilon} \leq 4.9v_0/d$ ;
- (v) the lower the impedance of the input bar, the greater the pressure measurement accuracy.

## Experiments

Selected dynamic experiments are carried out to demonstrate the proposed experimental technique. Technical details of the bulge testing system are given along with the experimental results. Moreover, the choice of the Hopkinson bar system is discussed.

### Material

The dynamic bulging experiments were performed on 1 mm thick 6111-T4 aluminum sheets. According to the test results presented in Yang et al. [24], the static stress–strain curve for this material may be approximated by Hollomon’s exponential law

$$s(\bar{\epsilon}_p) = k(\epsilon_{yp} + \bar{\epsilon}_p)^n \quad (26)$$

with the parameters  $k=535$  MPa,  $\epsilon_{yp}=0.18\%$  and  $n=0.226$ . The corresponding stress–strain curve is depicted in Fig. 4 (curve labeled ‘static’).

### Choice of the Viscoelastic SHPB System

The bulge cell diameter  $d$  should be large as compared to the sheet thickness in order to provide optimal stress and strain field homogeneity through the sheet thickness. At the same time, the cell diameter should be small to attain large strain rates at realistic striker velocities. Here, we chose a diameter of  $d=40$  mm which corresponds to a diameter-to-thickness ratio of  $d/h_0=40$ . According to equation (7), the expected pressure for bulging the aluminum specimen is  $p_{alu} \cong 18$  MPa at  $\bar{\epsilon}_p = 0.2$ . In order to choose the base material for the Hopkinson bar system, we evaluate the uncertainty of this pressure measurement at a strain rate of  $\bar{\epsilon}_p = 200\text{s}^{-1}$  for different input bars; five different bar materials are considered: tungsten, steel, titanium, aluminum and nylon (see Table 1). As described in ‘‘Plastic Strain Rate’’, the strain rate depends on the bar materials. Hence, the striker velocity needs to be adjusted to the bar material in order to achieve the same strain rate on different testing systems. The same properties are chosen for the output bar and the input bar, i.e.  $E_{out}=E_{in}$ ,  $\rho_{out}=\rho_{in}$  and  $A_{out}=A_{in}$ . When neglecting the inertia

of the bulge cell (limiting case of  $M \rightarrow 0$ ), we obtain from combining equations (10) and (20) that

$$v_0 = \frac{\dot{\bar{\epsilon}}_p d}{4.9} + 4 \frac{h_0}{d} \frac{s_0}{\sqrt{\rho_{in} E_{in}}} \quad (27)$$

where  $s_0 = s(\bar{\epsilon}_p = 0.2) = 372$  MPa for the aluminum specimens. The corresponding velocities for different bar materials are given in column 6 of Table 1. Next, we calculate the strain level of the incident wave based on equation (11), before estimating the uncertainty in the pressure measurement (see rightmost column in Table 1), assuming an uncertainty of  $\delta\epsilon = 1 \times 10^{-5}$  in the measured incident strain wave.

The results show that high impedance materials such as tungsten and steel, require a significantly lower impact velocity than low impedance bar materials such as nylon in order to achieve the same strain rate. At the same time, the strain induced by the incident wave in those materials is by one order of magnitude smaller. Consequently, the relative uncertainty  $\delta\epsilon/|\epsilon_{in}|$  in the incident wave measurement is much larger. The measurement error becomes even much larger when considering the pressure, since for high impedance materials, more than 80% of the incident wave is reflected at the specimen boundary. This results in pressure measurement uncertainties of more than 5% for all metallic bar materials listed in Table 1. Consequently, nylon bars are chosen to perform the dynamic tests on the Al6111-T4 alloy. For this testing system, the estimated pressure measurement uncertainties are below 0.3%. It is also worth noting that the total duration of an experiment with nylon bars may be much longer than with metallic bars because of the lower wave speed.

In addition to their low impedance, nylon bars exhibit a viscoelastic behavior. Therefore, the wave dispersion due to

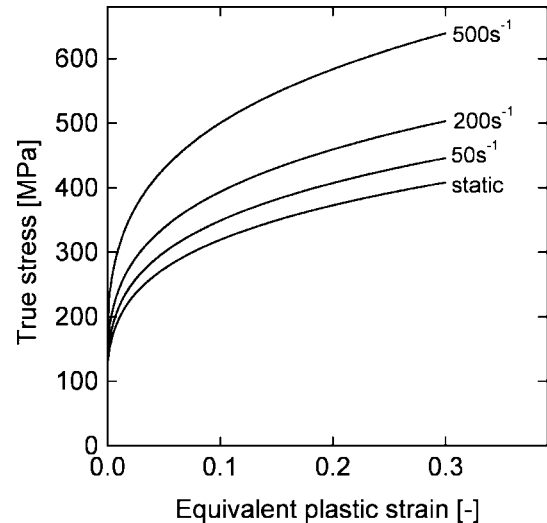


Fig. 4 Hollomon–Copper–Symonds material model of the Al6111-T4 alloy

**Table 1** Estimation of the pressure measurement accuracy for different Hopkinson bar systems at a strain of  $\bar{\epsilon}_p = 0.2$  and strain rate of  $\dot{\bar{\epsilon}}_p = 200\text{s}^{-1}$

	$E$ (GPa)	$\rho$ (g/cm <sup>3</sup> )	$c$ (m/s)	$\sqrt{E\rho}$ (MPa/m/s)	$v_0$ (m/s)	$\epsilon_t$ ( $\times 10^{-5}$ )	$\chi$ [-]	$\delta p/ p $ (%)
Tungsten	406	19.2	4598	88.3	2.1	-22.3	-0.80	31.9
Steel	210	7.8	5189	40.5	2.6	-24.6	-0.65	16.5
Titanium	100	4.7	4613	21.7	3.4	-36.3	-0.50	7.9
Aluminum	70	2.7	5092	13.7	4.3	-42.6	-0.40	5.5
Nylon	3.6	1.15	1769	2.0	19.9	-563.6	-0.11	0.3

viscous effects must be taken into account in addition to the geometric dispersion. This is of particular importance when calculating the waves at the input bar/fluid interface based on the measurement at the center of the input bar. Here, we made use of the DAVID software package [5] to calculate all waves. A brief overview of the computational procedure used by DAVID is given in Appendix A.

#### Details on the Experimental Set-up

Figure 5 shows a photograph of the bulge cell which is mounted on the  $d=40$  mm diameter input bar. The cylindrical bulge cell is  $a=100$  mm long and has a wall thickness of  $b=20$  mm [see Fig. 2(b) for dimension labels]. The total weight of the bulge cell (excluding the sheet specimen and fluid) is  $M=2,600$  g. The inner diameter of the die ring is  $e=36$  mm, while the corner radius of  $r=7$  mm increases the ring diameter to 50 mm at the contact surface with the sheet material [Fig. 2(b)]. Similarly, the inner diameter of the bulge cell is 50 mm at the contact surface with the sheet specimen, but it narrows down to 40 mm towards the input bar end. The contact surface of the die ring is grooved to guarantee the slip free clamping of the sheet specimen. Eight M8-12.9 socket cap screws are used to apply the clamping pressure to the die ring.

The input bar is inserted into the cylindrical cell before injecting 50 ml water through a lateral hole in the bulge cell. Water is chosen rather than oil because of its higher

bulk modulus and wave speeds, notably at high frequencies. After injecting the water, the input bar is advanced manually until all air has escaped from the fluid reservoir of the bulging cell; subsequently, the hole is closed using a fine threaded M6 screw. In order to match the contact surface of the die ring, the cross-section of the cylindrical output bar changes its shape to a tubular section along a distance of about 100 mm (see part #1 in Fig. 5). The total cross-sectional area is kept constant ( $A_{out}=A_{in}=1257$  mm<sup>2</sup>) along this transition length to reduce the effect of spurious wave reflections within the output bar.

The input bar has a total length of  $l_{in}=3070$  mm while the output bar is  $l_{out}=1919$  mm long. Thus, along with a  $l_s=1004$  mm long striker bar of the same diameter, experiments of a maximum duration of about  $2l_s/c_{in}=1130$   $\mu\text{s}$  can be performed. The strain gages on the input and output bars are positioned at a distance of 1537 mm and 500 mm from the respective interfaces with the bulge cell. The two strain signals are recorded at a frequency of 1 MHz. The theoretical strain gage sensitivity is validated for each experiment by evaluating the conservation of linear momentum between the striker and input bar. The impact velocity is measured using a laser/photodiode sensor in conjunction with a high contrast grating on the striker bar.

#### Experimental Results

A total of 12 experiments have been performed for striker speeds ranging from 13.8 m/s to 19.5 m/s. In the following subsections, we discuss selected representative results of this dynamic testing series.

#### Measured waves

The solid curves in Fig. 6 show the measured strain signals for a test performed at  $v_0=18.8$  m/s after transporting the waves to the bulge cell boundaries according to the procedure described in Appendix A. The incident compressive wave rises to its plateau strain level of about  $500 \times 10^{-5}$  during a time interval of about 140  $\mu\text{s}$ . The time profile of the reflected wave is of triangular shape in the tensile range; it exhibits a local maximum at a tensile strain of about

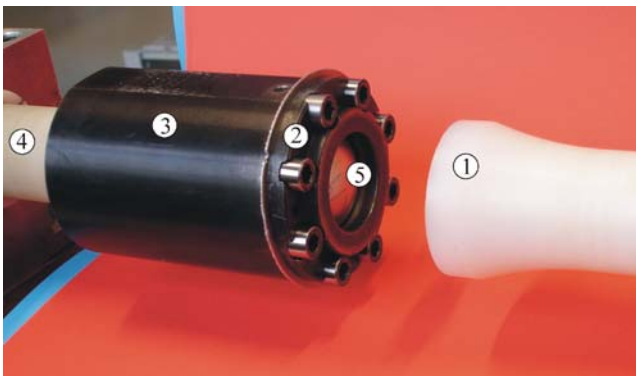


**Fig. 5** Photograph of the bulge cell: (1) output bar, (2) die ring, (3) bulge cell cylinder, (4) input bar, and (5) specimen (after testing)



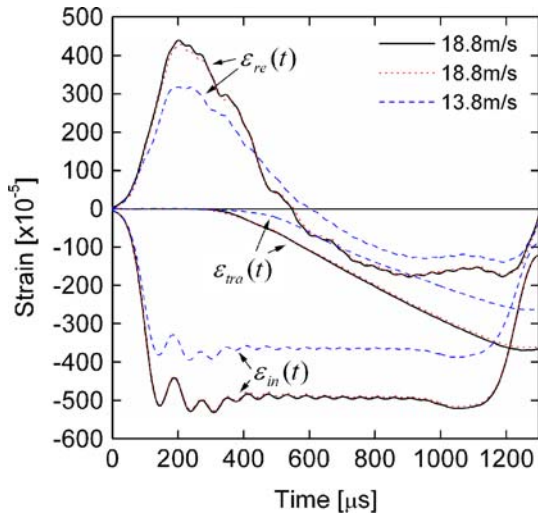


**Fig. 6** A set of three waves (incident, reflected, and transmitted wave) is shown for three different experiments (solid, dotted and dashed curves). The strain signals are shown for a frequency content of up to 60 kHz

$436 \times 10^{-5}$  after 206  $\mu\text{s}$ . The reflected wave becomes negative after a duration of about 550  $\mu\text{s}$ . After another 300  $\mu\text{s}$  the reflected wave remains more or less constant which is due to the compensation of material strain hardening by the geometrical changes that soften the specimen resistance (notably sheet thinning). The amplitude of both the reflected and incident wave decreases after about 1200  $\mu\text{s}$ , which corresponds to the duration of a round-trip for a wave propagating in the 1004 mm long striker bar. The results from a second experiment at the same striker velocity are also shown in Fig. 6 (dotted red curves). The comparison of the measured waves demonstrates the good repeatability of the dynamic bulge experiment. Furthermore, the waves for an experiment at 13.8 m/s are shown as dashed blue curves. The strain levels are considerably different, but there are only little differences from a qualitative point of view.

#### Velocity-time histories

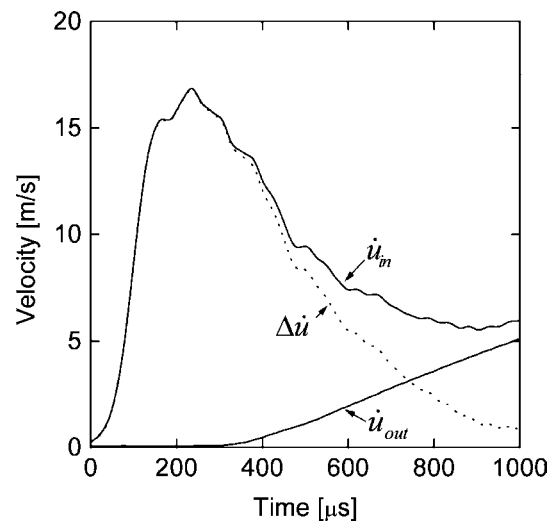
Figure 7 shows the velocity-time histories which have been calculated from the measured strain histories at 18.8 m/s. The input velocity reaches its maximum of  $\dot{u}_m \cong 16.8 \text{ m/s}$  at 245  $\mu\text{s}$  after impact. The output bar velocity is still negligibly small at that time which indicates that the soft initial response of the specimen along with the inertia of the bulge cell delays the acceleration of the output bar. The output bar sets in motion long after the input velocity has reached its maximum; it attains 10% of the input velocity after about 470  $\mu\text{s}$ . The time history of the effective piston velocity (dashed line in Fig. 7) follows closely the evolution of the input velocity, but decreases to zero towards the end of the experiment.

#### Pressure-time histories

The fluid pressure is evaluated according to equation (1). Figure 8(a) shows a plot of the pressure-time history; during the first 200  $\mu\text{s}$  of the experiment, the pressure-time curve exhibits a pronounced initial peak before the pressure level increases almost monotonically until it reaches its maximum after about 1100  $\mu\text{s}$ ; subsequently, the pressure level decreases because of the end of the incident wave. The maximum pressures are about 25 and 17 MPa for the experiments carried out at striker velocities of 18.8 and 13.8 m/s, respectively. As demonstrated in Appendix B, the pronounced initial peak is due to the fact that the pressure is determined at the input bar/water interface instead of the water/specimen interface.

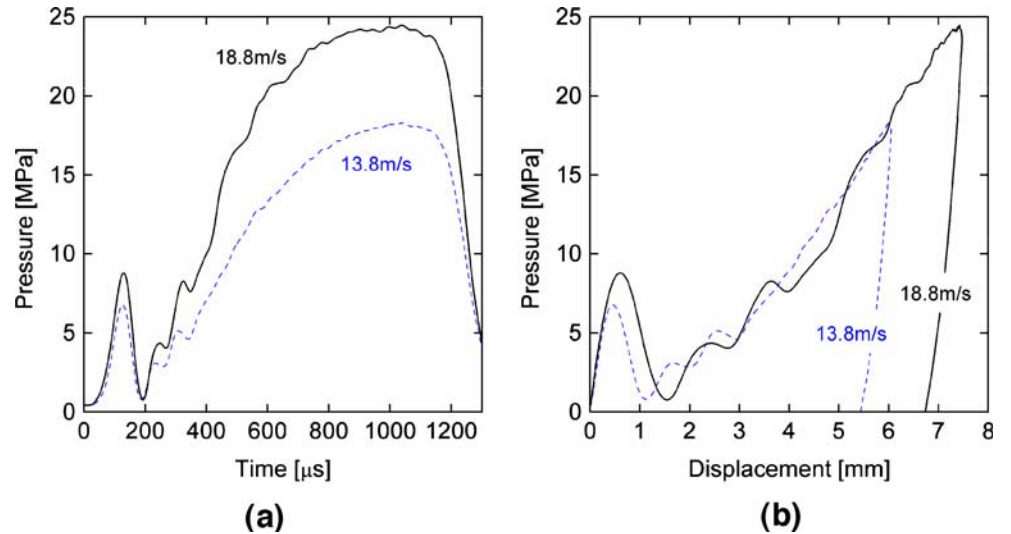
#### Pressure-displacement histories

Figure 8(b) shows the pressure at the input bar/water interface as a function of the effective piston displacement. Following the initial pressure peak, the pressure-displacement curves increase in a more or less linear manner. This observation compares well with the simple theoretical solution depicted in Fig. 3. The beginning of the linear post-peak regime may be considered as the point where the specimen response changes from bending-dominated to membrane-dominated. An effective displacement of about 1 mm may be associated with that point which corresponds to the thickness of the aluminum sheet material. A maximum displacement of 7.5 mm is reached at a striker velocity of 18.8 m/s, whereas the experiment at 13.8 m/s terminates at 6.0 mm. It is worth noting that both curves are very close for large displacements, while low frequency oscillations seem



**Fig. 7** History of the cross-sectional velocities at the interfaces between the bulge cell and the Hopkinson bar system (solid curves). The dashed curve depicts the effective piston displacement which corresponds to the difference of the input and output velocity profile

**Fig. 8** (a) Fluid pressure-time history at the input bar/fluid interface, and (b) fluid pressure versus effective piston displacement curve for striker velocities of 13.8 m/s (*dashed curves*) and 18.8 m/s (*solid curves*)



to affect the response at effective piston displacements below 5 mm.

### Numerical Simulations and Inverse Analysis

A finite element model of the dynamic bulging experiment was constructed and used to determine the rate-dependent material model properties for the aluminum sheets from inverse analysis. The idea is to apply the measured incident wave as a boundary condition when calculating the specimen response. The parameters of a Cowper–Symonds material model are then calibrated in an iterative procedure to provide the best estimate of the pressure- and displacement-time histories.

#### Computational Model of the Viscoelastic Bars

In the case of transversely isotropic sheet materials, an axisymmetric model may be used for the analysis. The bars are discretized by first-order axisymmetric elements of  $l_e = 2$  mm edge length along the bar axis. The computational input bar must be sufficiently long to avoid any alteration of the incident wave by returning reflected waves. In the present finite element model, the lengths of the input and output bars are  $l_{in} = 1500$  mm and  $l_{out} = 800$  mm, respectively. It is expected that waves of frequencies of up to about  $c_{in}/20l_e \cong 40$  kHz can be represented by the FE-model which corresponds well to the range of frequencies observed in the experiments.

The bar mesh comprises only one element row in the radial direction. The bar materials are modeled as linear elastic with the Young’s moduli  $E_{in} = E_{out} = 3.6$  GPa and the mass densities  $\rho_{in} = \rho_{out} = 1.145$  g/cm<sup>3</sup>. At the same time, the Poisson ratios are set to a non-physical value of  $\nu = 0$ . Thus, uniaxial waves in the computational model are not altered

when traveling along the bar axis. Instead of approximating the geometrical and material-induced wave dispersion by an advanced finite element model, we modified the model boundary conditions to account for the wave dispersion in the viscoelastic bars. More specifically, we make use of the exact theoretical solution of the wave equation (see Appendix A) to calculate the dispersed velocity-time history of the incident wave at the input bar/water interface based on the experimentally-measured strain history near the center of the input bar. When applying this dispersed velocity-time history to the nodes at the free end of the model input bar, the same velocity profile arrives at the input bar/water interface because the computational model does not account for Poisson deformation (recall that  $\nu = 0$ ) nor for viscous effects.

#### Finite Element Model of the Bulge Cell and the Bar Interfaces

The axisymmetric finite element discretization of the bulge cell is shown in Fig. 9. All geometric entities are modeled using 4-node axisymmetric elements with reduced integration (element #15 of the LS-DYNA library, Livermore Software Technology Corporation [10]) and Belytschko–Bindeman hourglass control (stiffness-based). The sheet material is discretized with three elements through-the-thickness. The steel parts of the bulge cell are modeled as linear (hypo-)elastic with the Young’s modulus  $E = 210$  GPa, Poisson’s ratio  $\nu = 0.3$ , and mass density  $\rho = 7.85$  g/cm<sup>3</sup>. The water is modeled as linear elastic fluid with the bulk modulus  $K = 2.5$  GPa and the mass density  $\rho = 1.0$  g/cm<sup>3</sup>. A power law J2-plasticity model is used for the aluminum sheet material to approximate the stress–strain relationship given by equation (26) (model #18 of the LS-DYNA material library). Furthermore, based on previous experimental studies on the rate sensitivity of aluminum

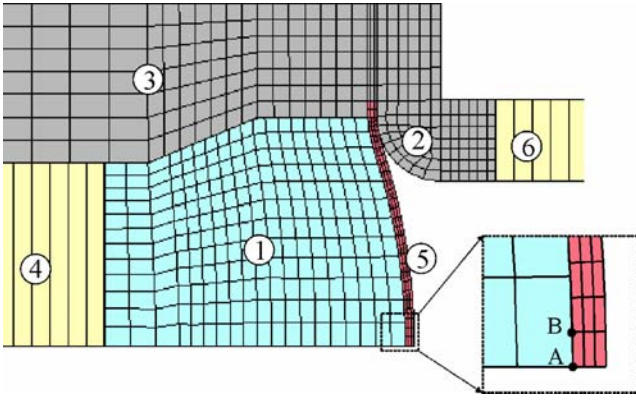


**Fig. 9** Axisymmetric finite element mesh showing the (1) water, (2) the die ring, (3) a part of the bulge cell cylinder, (4) a part of the input bar, (5) the sheet specimen, and (6) a part of the output bar. The detail in dashed lines shows the position of the nodes 'A' and 'B' which have been used to calculate the strain near the specimen center

(e.g. Jones [9]), a phenomenological Cowper–Symonds approach is taken to model the effect of strain-rate. The strain rate dependent phenomenological expression for the deformation resistance reads

$$s(\bar{\epsilon}, \dot{\bar{\epsilon}}_p) = k(\epsilon_{yp} + \bar{\epsilon}_p)^n \left[ 1 + \left( \frac{\dot{\bar{\epsilon}}_p}{C} \right)^{\frac{1}{q}} \right] \quad (28)$$

where  $C$  and  $q$  denote the Cowper–Symonds coefficients.

The two-dimensional automatic surface-to-surface penalty contact algorithm of the LS-DYNA v970 library is employed to model the friction-free interaction between all components of the testing system. Before calibrating the rate-dependent material model, a first set of simulations is performed using the rate-independent material model ( $C \rightarrow \infty$ ). The resulting pressure–displacement curve for 18.8 m/s is shown by a thin dotted line in Fig. 10.

#### Inverse Analysis

An inverse analysis software package [21] is used to determine the Cowper–Symonds coefficients. The pressure-time history  $p(t)$  and the effective displacement-time history  $\Delta u(t)$  are chosen to define the objective function  $\psi = \psi(C, q)$  of the inverse analysis algorithm. Using the superscripts 'FEA' and 'EXP' to distinguish between simulation results and experimental measurements, we write

$$\psi(C, q) := \frac{1}{\tilde{p}^2} \sum_{i=0}^N [p_i^{EXP} - p_i^{FEA}(C, q)]^2 + \frac{1}{\tilde{u}^2} \sum_{i=0}^N [\Delta u_i^{EXP} - \Delta u_i^{FEA}(C, q)]^2 \quad (29)$$

where  $p_i = p(t_i)$  and  $\Delta u_i = \Delta u(t_i)$ ; the weighting parameters  $\tilde{p}$  and  $\tilde{u}$  are introduced to normalize the pressure and

displacement residuals. Denoting the total duration of the experiment by  $T$ , we have  $t_i = iT/N$  while  $N+1$  corresponds the total number of discrete time measurements throughout the experiment (sampling frequency  $N/T$ ).

The optimal Cowper–Symonds coefficients  $C_m$  and  $q_m$  are found from minimizing the objective function

$$(C_m, q_m) = \arg \min_{(c, q)} \{\psi(C, q)\}. \quad (30)$$

This minimization is carried out using the gradient method of Levenberg–Marquardt [21].

The experimental results for 13.8 m/s and 18.8 m/s are used to determine the Cowper–Symonds coefficients. The optimization is performed for  $N=250$ . The weighting parameters are set to  $\tilde{p} = 1 \text{ MPa}$  and  $\tilde{u} = 1 \text{ mm}$ , which attributes a larger weight to the pressure residual (note that the pressure reaches values of up to 24 MPa, while the effective displacement remains inferior to 8 mm). The starting values  $C=6.5 \times 10^3$  and  $q=4.0$  are chosen for the inverse analysis (values given for aluminum in Jones [9]). The inverse analysis procedure required 15 iterations (FE-simulation runs) to determine the “optimal” Cowper–Symonds coefficients of  $C_m=8.3 \times 10^3$  and  $q_m=2.15$ . The corresponding effect on the stress–strain curve is illustrated in Fig. 4.

The dashed curve in Fig. 10 shows the pressure–displacement curves as obtained from finite element simulations performed with the rate-dependent Cowper–Symonds material model. Due to the particular choice of the objective function [equation (30)], the optimized rate-dependent model yields good agreement for large pressures and displacements, whereas more pronounced deviations between the experiments and the model are detectable at an earlier stage of the experiment.

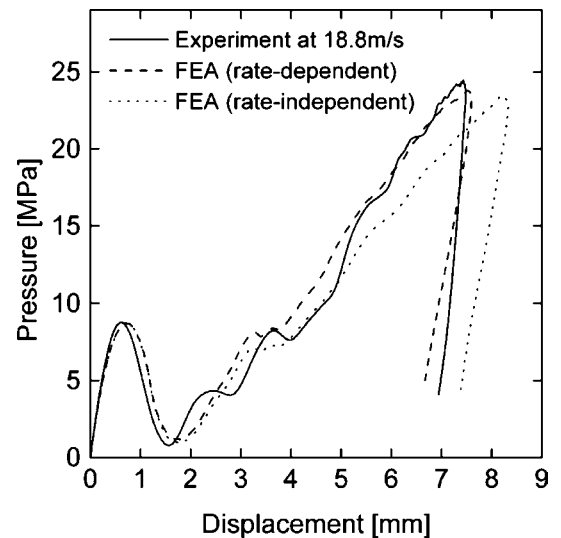


**Fig. 10** Comparison of the finite element simulation results with the experimentally measured pressure versus effective displacement curve for 18.8 m/s

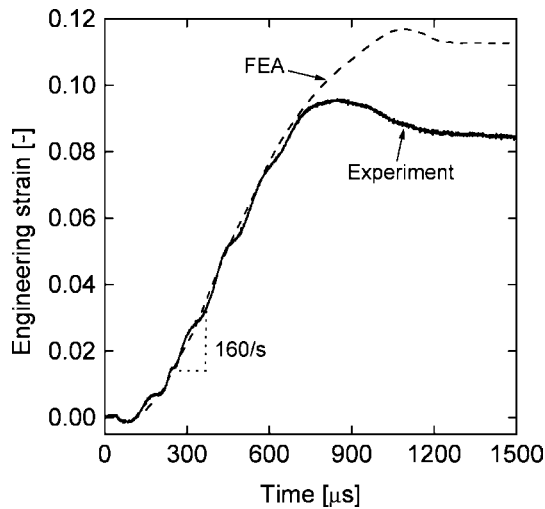


**Fig. 11** Engineering membrane strain at the inner surface of the bulge specimen as a function of time for a loading velocity of 17.7 m/s

### Validation of Local Strains and Strain Rate

In addition to comparing the simulated and measured pressure–displacement histories, we make use of local strain measurements to validate the computational model. A large deformation strain gage (model KFEL 5-120-C1, Kyowa, Japan) is attached to the inner surface of the sheet specimen. The inner surface is chosen rather than the outer surface because the superposed fluid pressure reduces the risk of delamination for the strain gage. The strain gage measures the strain over a length of 5 mm at the center of the bulge. The solid curve in Fig. 11 shows the engineering membrane strain versus time history as measured throughout a bulge tests at 17.7 m/s. It increases linearly at an average slope of about  $160 \text{ s}^{-1}$  until the strain gage detaches from the specimen surface at strain of about 0.09. The strain curve labeled ‘FEA’ is determined from the relative displacement of the nodes ‘A’ and ‘B’ at the inner surface of the specimen (see detail in Fig. 9). It compares well to the experimental result over the entire measurement range. Beyond the measurement range, it increases up to a maximum membrane strain of almost 12% before unloading elastically.

*Aside* It is worth noting that both the equivalent plastic strain and the equivalent plastic strain rate are approximately twice as large as their membrane counterparts. In other words, in the present experiment, the dominant equivalent plastic strain rate is about  $\bar{\epsilon}^p = 320 \text{ s}^{-1}$ .

### Discussion

A new experimental method has been proposed and validated for the dynamic biaxial testing of sheet metal

specimens. The material properties are identified using an inverse method. Therefore, in addition to the reliability of the experimental measurements, the reliability of the finite element model is critical. It is common practice in static bulge testing to measure the curvature of the bulge (e.g. [19]); knowing the curvature and the bulging pressure, the membrane stresses can be computed according to simple membrane theory. Furthermore, the strain field is typically measured using digital image correlation (DIC). Thus, the static biaxial stress–strain curve is directly found from measurements without running finite element simulations.

Conceptually, the same procedure could also be adapted to the dynamic loading case. From a practical point of view, these additional measurements are challenging, but feasible when using lasers to measure the curvature and DIC on a small area at the center of the specimen. However, this procedure will rely heavily on the membrane assumption of the underlying theoretical model which may provide a poor approximation in the dynamic case. For instance, the history plot of the equivalent plastic strain at different positions along the sheet thickness direction (Fig. 12) reveals that bending plays a non-negligible role in the present experiment. Choosing a larger specimen diameter (as it is typically done in static bulge tests) would improve the strain homogeneity along the thickness direction, but this option is not viable in the dynamic case. Recall that the strain rate is roughly proportional to the striker velocity-to-diameter ratio [see equation (20)]. Thus, in order to maintain the level of strain rate, the impact velocity needs to be increased accordingly. However, since the wave

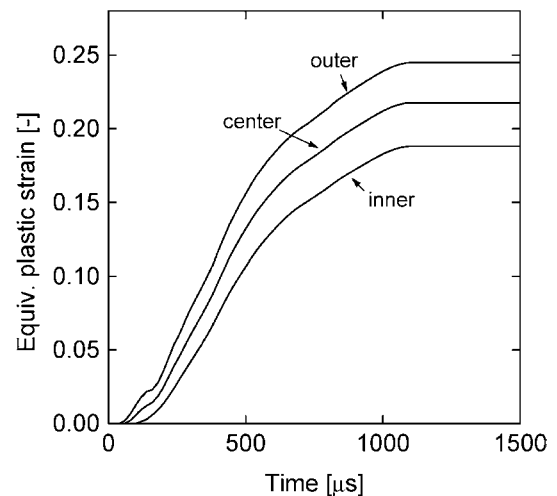


**Fig. 12** Evolution of the equivalent plastic strain at the specimen center at different positions in the thickness direction. The curves correspond to the results at the integration points of the three elements through the sheet thickness (loading velocity of 17.7 m/s). The curve labeled ‘inner’ depicts the results for the element which is in contact with the water

propagation speeds within the fluid may not be altered, transient effects within the fluid are likely to become dominant. In particular, it may be expected that the pressure distribution would no longer be homogeneous and hence, the entire analytical procedure of calculating the stress–strain relationship from experimental measurements would break down. Note that for the present bulge cell dimensions, a pressure wave takes about 12  $\mu\text{s}$  to travel from the specimen center to the cell boundaries.

Based on these arguments, we favor the development of reliable hybrid experimental–numerical methods for dynamic bulge testing. Another advantage of this approach is its applicability to anisotropic materials. However, from an experimental point of view, additional measurements such as the fully three-dimensional displacement field throughout bulging are recommended for future studies. These measurements could enhance the reliability of the inverse calibration method and also eventually reveal model deficiencies, notably in the anisotropic case. It is emphasized that the present work focuses on the design and feasibility of a dynamic bulge test, whereas future research must address the material model identification procedure in more detail.

## Conclusion

A dynamic bulge testing cell is developed to perform biaxial tensile tests on a SHPB system. The original idea is to make use of the input bar to apply and measure the fluid pressure. Careful analysis of the proposed testing system demonstrates that conventional metallic bar systems cannot provide sufficient measurement accuracy. Instead, low impedance input bars must be employed.

A series of dynamic experiments were carried out on 1 mm thick aluminum 6111-T4 sheets at an equivalent plastic strain rate of about 300  $\text{s}^{-1}$ . The design of the bulge cell is described and the experimental results are discussed in detail. A custom-made nylon input bar is used to achieve a pressure measurement uncertainty of less than 0.5%. A finite element model of the testing system is built and used to determine the parameters of the rate-dependent Hollomon–Cowper–Symonds J2-plasticity model through inverse analysis. It may be concluded that the proposed dynamic bulge testing technique provides an attractive alternative to conventional dynamic tensile tests. The proposed experimental procedure is more reliable than direct tension tests because it circumvents the inherent gripping and force measurement issues associated with direct tension tests. However, in order to fully benefit from this new experimental technique, a more rigorous approach to the inverse determination of rate-dependent material laws needs to be developed.

**Acknowledgement** The partial support by the program “De la mise en forme au comportement dynamique” of the Région Bretagne is gratefully acknowledged. The authors wish to thank Mr. R. Barre from LMS, Mr. H. Bellegou from LG2M and Mr. F. Portanguen from UBS University for their technical assistance.

## Appendix A

### Wave Transportation in Viscoelastic Bars

In SHPB experiments, the strains at the specimen/bar interfaces are calculated based on the strain measurements at a different position along the bar axis (e.g. near the center of the input bar). In the following, we will briefly describe the “wave transportation” procedure for viscoelastic bars where both structural and material-induced wave dispersion need to be taken into account. The proposed procedure follows closely the theoretical developments presented by Zhao and Gary [25]. Note that we make use of the superscript “\*” to indicate complex variables.

In a viscoelastic bar, an uniaxial strain wave  $\varepsilon(x,t)$  propagating in the positive x-direction may be expressed by the Fourier representation

$$\varepsilon(x,t) = \int_{-\infty}^{\infty} A^*(\omega) e^{i \left[ \xi^* x - \omega t \right]} d\omega \quad (31)$$

where  $\omega$  denotes the wave frequency. The complex wave number  $\xi^* = \xi^*(\omega)$  is defined as

$$\xi^*(\omega) = \frac{\omega}{c(\omega)} + i\alpha(\omega) \quad (32)$$

where the functions  $c(\omega)$  and  $\alpha(\omega)$  represent the phase velocity and damping, respectively. Both functions depend on the bar diameter and the viscoelastic bar material properties. An identification procedure for the experimental determination of  $c(\omega)$  and  $\alpha(\omega)$  is given in Othman et al. [14]. Figure 13 depicts these functions for the nylon bars used in the present study.

The frequency dependent function  $A^*(\omega)$  is determined from the strain measurement  $\varepsilon(x_0,t)$  at the position  $x=x_0$  (location of the strain gage). Using Fourier transformation,  $A^*(\omega)$  reads

$$A^*(\omega) = 2\pi e^{-i\xi^* x_0} \int_{-\infty}^{\infty} \varepsilon(x_0,t) e^{i\omega t} dt \quad (33)$$

After evaluating equations (33), (31) can be used to calculate the strain wave at any position along the bar axis. In the proposed experimental procedure, we make use of equation (31) to calculate the incident and reflected strain waves at the input bar/specimen interface ( $x=x_1$ ) based on



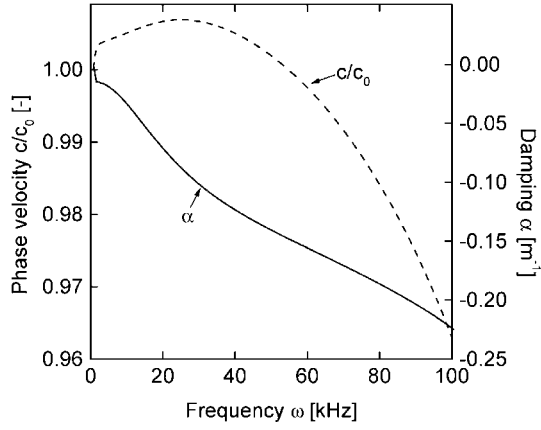


**Fig. 13** Normalized phase velocity and damping as a function of the frequency for the viscoelastic nylon bars

the strain measurement near the input bar center. Fast Fourier Transformation (FFT) and inverse FFT are used to evaluate these equations for discrete data. In a compact form, we may write

$$\varepsilon(x_1, t) = FFT^{-1} \left\{ FFT[\varepsilon(x_0, t)] e^{i\xi^* \Delta x} \right\} \quad (34)$$

where  $\Delta x = x_1 - x_0$  when transporting the incident wave and  $\Delta x = x_0 - x_1$  in the case of the reflected wave (which travels in the negative x-direction).

## Appendix B

### Origin of the Initial Pressure Peak

The pronounced initial peak is due to the fact that the pressure is determined at some distance  $w$  from the specimen boundary [Fig. 2(b)]. Note that the specimen boundary is defined by the fluid/sheet metal interface, whereas the SHPB system determines the pressure at the input bar/fluid interface. Both the density and modulus of nylon and water are very similar. Thus, we can make use of a simple model to explain the initial pressure in which we assume the same modulus and density for the water and nylon.

At the beginning of the experiment, the non-linear specimen response is very soft. In other words, the fluid/specimen interface ( $x=x_2$ ) acts like a (stress-) free boundary where the incident wave  $\varepsilon_i(x_2, t)$  is fully reflected. Formally, we write

$$p(x_2, t) = E_{in}[\varepsilon_i(x_2, t) + \varepsilon_r(x_2, t)] = 0 \quad (35)$$

and hence

$$\varepsilon_r(x_2, t) = -\varepsilon_i(x_2, t). \quad (36)$$

At the input bar/fluid interface ( $x=x_1$ ), the waves are shifted in time. The incident wave passes this interface earlier, i.e.

$$\varepsilon_i(x_1, t) = \varepsilon_i(x_2, t + \Delta t). \quad (37)$$

where  $\Delta t = w/c_{in}$ . Conversely, the reflected wave is delayed,

$$\varepsilon_r(x_1, t) = \varepsilon_r(x_2, t - \Delta t) = -\varepsilon_i(x_2, t - \Delta t). \quad (38)$$

Thus, instead of measuring zero pressure, the pressure at the input bar/fluid interface is

$$\begin{aligned} p(x_1, t) &= E_{in}[\varepsilon_i(x_1, t) + \varepsilon_r(x_1, t)] \\ &= E_{in}[\varepsilon_i(x_2, t + \Delta t) - \varepsilon_i(x_2, t - \Delta t)] \end{aligned} \quad (39)$$

The incident strain increases monotonically in a non-linear manner until it has reached its plateau level. The pressure level at the incident bar/water interface keeps on increasing until the slope of the delayed reflected wave exceeds the slope of the incident wave. Thus, the condition

$$\frac{\partial \varepsilon_i(x_2, t^* + \Delta t)}{\partial t} - \frac{\partial \varepsilon_i(x_2, t^* - \Delta t)}{\partial t} = 0 \quad (40)$$

determines the time point  $t^*$  at which the initial pressure maximum is reached; Fig. 14 shows a sketch of the waves at the input bar/fluid interface. The superposition (solid blue curve) of the incident and reflected waves clearly shows the pressure peak according to this simple model. For an initial water layer thickness of  $w=39.5$  mm, we have  $\Delta t = w/c_{in} = 22$   $\mu\text{s}$ , while  $t^* \approx 95$   $\mu\text{s}$ . Observe from Fig. 8(a) that  $t^*$  is the same for the tests at 13.8 and 18.8 m/s. This is

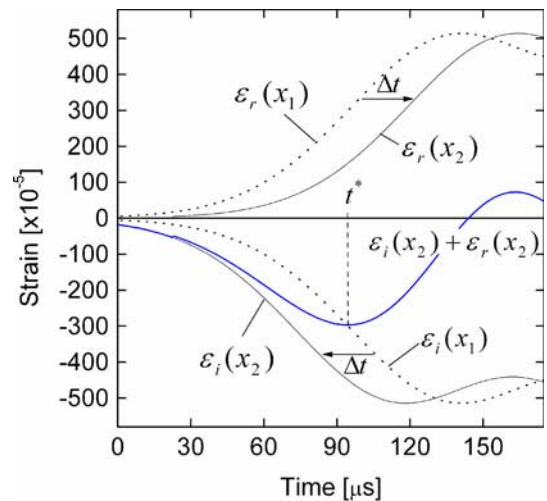


**Fig. 14** Wave superposition at the input bar/fluid interface ( $x=x_2$ ) based on the hypothesis of  $p=0$  at the fluid/sheet specimen interface ( $x=x_1$ )

consistent with equation (40): the incident wave amplitude is proportional to the impact speed and hence, it has no effect on the time point  $t^*$  given by equation (40). However, the corresponding peak pressure varies accordingly.

## References

1. Atkinson M (1997) Accurate determination of biaxial stress–strain relationships from hydraulic bulging tests of sheet metals. *Int J Mech Sci* 39(7):761–769.
2. Broomhead P, Grieve RJ (1982) Effect of strain rate on the strain to fracture of a sheet steel under biaxial tensile stress conditions. *J Eng Mater Technol* 104(2):102–106.
3. Brown WF Jr., Thompson FC (1949) Strength and failure characteristics of metal in circular bulging. *Trans Am Soc Mech Eng* 71:575–585.
4. Chakrabarty J, Alexander JM (1970) Hydrostatic bulging of circular diaphragms. *J Strain Anal* 5(3):155–161.
5. Gary G (2005) DAVID instruction manual, Palaiseau, France <http://www.lms.polytechnique.fr/EQUIPE/dynamique/index.html>.
6. Gleyzal A (1948) Plastic deformation of a circular diaphragm under pressure. *J Appl Mech* 70:288–296.
7. Gutscher G, Wu H-C, Ngai G, Altan T (2004) Determination of flow stress for sheet metal forming using the viscous pressure bulge (VPB) test. *J Mater Process Technol* 146(1):1–7.
8. Hill R (1950) A theory of the plastic bulging of a metal diaphragm by lateral pressure. *Philos Mag* 4(322):1133–1142.
9. Jones N (1997) *Structural impact*. Cambridge University Press.
10. Livermore Software Technology Corporation (2003) LS-DYNA 970 user's manuals. Livermore Software Technology Corporation, Livermore.
11. Mahmudi R (1993) Forming limits in biaxial stretching of aluminium sheets and foils. *J Mater Process Technol* 37(1–4):203–216.
12. Nicholson ED, Field JE (1994) The mechanical and thermal properties of thin films. *J Hard Mater* 5:89–132.
13. NIST (1994) Guidelines for evaluating and expressing the uncertainty of NIST measurement results, NIST Technical Note 1297. NIST, Gaithersburg.
14. Othman R, Blanc RH, Bussac M-N, Collet P, Gary G (2002) Identification of the dispersion relation in rods, C.R. *Mecanique* 330:849–855.
15. Pickett AK, Pyttel T, Payen F, Lauro F, Petrinic N, Werner H, Christlein J (2004) Failure prediction for advanced crashworthiness of transportation vehicles. *Int J Impact Eng* 30(7):853–872.
16. Ranta-Eskola AJ (1979) Use of the hydraulic bulge test in biaxial tensile testing. *Int J Mech Sci* 21(8):457–465.
17. Rees DWA (1995) Instability limits to the forming of sheet metals. *J Mater Process Technol* 55(3–4):146–153.
18. Rees DWA (1995) Plastic flow in the elliptical bulge test. *Int J Mech Sci* 37(4):373–389.
19. Rees DWA (2001) Bi-axial pole strain transducer device. *Meas Sci Technol* 12(1):97–102.
20. Ross EW, Prager W (1954) On the theory of the bulge test. *Q Appl Math* 12(1):86–91.
21. SiDoLo (2003) User's manual (in French), Laboratoire Genie Mecanique et Materiaux, Universite de Bretagne Sud, Lorient, France.
22. Small MK, Nix WDF (1992) Analysis of the accuracy of the bulge test in determining the mechanical properties of thin films. *J Mater Res* 7(6):1553–1563.
23. Tsakalakos T (1981) The bulge test: a comparison of theory and experiment for isotropic and anisotropic films. *Thin Solid Films* 75:293–305.
24. Yang D-Y, Oh SI, Huh H, Kim YH (2002) Proceedings of the 5th International Conference and Workshop on Numerical Simulation of 3D Sheet Forming Processes. Elsevier, Amsterdam, pp 861–870.
25. Zhao H, Gary G (1995) A three dimensional analytical solution of the longitudinal wave propagation in an infinite linear viscoelastic cylindrical bar. Application to experimental techniques. *J Mech Phys Solids* 43(8):1335–1348.